


# Transition from band insulator to excitonic insulator via alloying Se into monolayer $\text{TiS}_3$ : A computational study

Shan Dong and Yuanchang Li <sup>\*</sup>

Key Laboratory of Advanced Optoelectronic Quantum Architecture and Measurement (MOE), and Advanced Research Institute of Multidisciplinary Science, Beijing Institute of Technology, Beijing 100081, China



(Received 27 May 2020; accepted 24 September 2020; published 14 October 2020)

First-principles density functional theory plus Bethe-Salpeter equation calculations are employed to investigate the electronic and excitonic properties of monolayer titanium trichalcogenide alloys  $\text{TiS}_{3-x}\text{Se}_x$  ( $x = 1$  and  $2$ ). It is found that the band gap and exciton binding energy display asymmetric dependence on the substitution of Se for S. While the band gap can be significantly decreased as compared to that of pristine  $\text{TiS}_3$ , the exciton binding energy varies slightly, regardless of the position and concentration of the Se substitution. A negative exciton formation energy is found when the central S atoms are replaced by Se atoms, suggesting a many-body ground state with spontaneous exciton condensation. Our work thus offers insight for engineering an excitonic insulator.

DOI: [10.1103/PhysRevB.102.155119](https://doi.org/10.1103/PhysRevB.102.155119)

## I. INTRODUCTION

An excitonic insulator was first proposed in the 1960s by theoretical physicists; this type of insulator has a many-body ground state with spontaneous exciton formation [1–6]. It has a macroscopic quantum state similar to BCS superconductors but results from a larger exciton binding energy than the energy gap. The nature of the excitonic insulator phase remains inconclusive although more than 50 years have passed and compelling experimental evidence is still lacking [7]. In recent years, the interest in excitonic insulator research has been reignited, partly by virtue of the vast progress in low-dimensional systems [8–15]. For instance, experimental evidence has been reported for a topological excitonic insulator in an InAs/GaSb quantum well structure [8] and for an exciton Bose-Einstein condensate at temperatures above 100 K in  $\text{MoSe}_2\text{-WSe}_2$  atomic double layers [9]. Theoretically, one-dimensional carbon nanotubes [11] and two-dimensional gallium arsenide [12], monolayer transition-metal chalcogenides [12,13] and halides [14], and semihydrogenated graphene [15] are predicted to be excitonic insulators on the basis of first-principles density functional theory plus Bethe-Salpeter equation (BSE) calculations. The studies in two-dimensional magnetic systems [14,15] imply that an exciton instability can even exist in wide-gap semiconductors with a one-electron gap  $>3$  eV, thus going beyond the conventional understanding that an excitonic insulator transition occurs in small gap semiconductors or semimetals [5].

Monolayer  $\text{TiS}_3$  is one kind of transition-metal trichalcogenide, which has been fabricated by exfoliation from its layered material [16]. It has a direct gap around 1 eV with a high carrier mobility and may find applications in future nanoelectronics, thermoelectric devices, and infrared light

emission [17–19]. Due to its two-dimensional nature, the screening of the electron-hole interaction is significantly reduced in monolayer  $\text{TiS}_3$ , leading to a large exciton binding energy [12,20–23]. Even more interesting is that its band-edge states have the same parity and thus transitions between them are dipole forbidden, which further suppresses the screening effect. As a consequence, a ground-state dark exciton is predicted to have a binding energy just  $\sim 0.3$  eV smaller than a one-electron band gap [12]. Under moderate compressive strain, the exciton binding energy would exceed the band gap, hence realizing a phase transition from a band insulator to an excitonic insulator.

Alloying is another widely used method to tailor the electronic and magnetic properties of solid state materials for designing specific applications [24–36]. This has been well established for transition-metal dichalcogenides [34–36], e.g.,  $\text{MoS}_{2-x}\text{Se}_x$ ,  $\text{Mo}_{1-x}\text{W}_x\text{S}_2$ ,  $\text{TiS}_{2-x}\text{Se}_x$ ,  $\text{Nb}_{1-x}\text{Re}_x\text{S}_2$ , etc. Recently, alloying a fraction of Se into  $\text{TiS}_3$  has also been experimentally demonstrated by Agarwal *et al.* [37]. While current success is limited to alloys with a minuscule amount (8%) of Se, their energetic calculations on  $\text{TiS}_{3-3x}\text{Se}_{3x}$  showed that the stable alloy composition is located at a much higher amount  $x = 1/3$ . Isoelectronic substitution of S with Se not only can tune the system's band gap as usual but would also generate a so-called chemical pressure which thus may drive the alloy into an intrinsic excitonic insulator state.

In this paper, we investigate the effect of Se-to-S substitution on the electronic and excitonic properties of a  $\text{TiS}_3$  monolayer, especially the changing trend of the band gap relative to the exciton binding energy, using first-principles calculations coupled with the BSE. It is found that the S atoms of  $\text{TiS}_3$  located at the middle and the side have substantially different contributions to the band-edge states, consequently leading to very different substitution effects. Substituting the middle S with Se significantly reduces the band gap while substituting the side S causes less of an effect. On the contrary, the

<sup>\*</sup>yuanchangli@bit.edu.cn

introduction of Se almost has no effect on the exciton binding energy regardless of what kind of S is substituted, manifesting itself as a unique two-dimensional screening behavior. This disproportionate change between the band gap and exciton binding energy can eventually cause a phase transition from a band insulator to an excitonic insulator as a result of the exciton binding energy exceeding the corresponding band gap when the substitution occurs for the middle S atoms.

## II. METHODOLOGY AND MODELS

Geometric optimizations and electronic structure calculations were performed using the Perdew-Burke-Ernzerhof (PBE) [38] exchange-correlation function within the framework of density functional theory as implemented in the QUANTUM ESPRESSO code [39]. The Heyd-Scuseria-Ernzerhof (HSE06) hybrid functional [40] was further used for the band-gap calculations on top of the PBE optimized structures. After a convergence test, a 60-Ry cutoff was set for optimized norm-conserving Vanderbilt pseudopotentials [41]. A vacuum layer of more than 15 Å was used along the out-of-plane direction to avoid spurious interactions between adjacent layers. A  $12 \times 16 \times 1$   $k$ -point grid was used for the geometric optimization and all structures were fully relaxed until the residual force on each atom was less than 0.01 eV/Å. A fine  $18 \times 24 \times 1$   $k$ -point grid was adopted for energetic and electronic structure calculations. The BSE was solved for the excitonic properties by using the YAMBO code [42]. The same fine  $k$ -point grid, 88 bands, and 12-Ry cutoff were used to calculate the dielectric function matrix. The top five valence bands and bottom two conduction bands were chosen to build the BSE Hamiltonian. The Coulomb cutoff technique was employed in the BSE calculations to avoid an artificial interaction between the periodic adjacent layers. Because of the current unaffordable computational cost for a fully converged solution of BSE at the HSE level, the PBE band gap is corrected to the HSE values by applying a scissor operator for both the response function and diagonal part of the BSE kernel [43]. The geometric structures were illustrated with VESTA [44] in the figures.

## III. RESULTS AND DISCUSSION

Monolayer  $\text{TiS}_3$  possesses inversion symmetry and a unit cell is composed of two Ti and six S atoms. It takes a rectangle structure in the basal plane with optimized lattice constants  $a_1 = 5.017$  Å and  $a_2 = 3.413$  Å, and has a quintuple-layer structure with S-Ti-S-Ti-S atomic layers stacked along the vertical direction, as shown in Fig. 1. There are two kinds of S atoms: One is at the side ( $S^S$ ) and the other is at the middle ( $S^M$ ).

Shown in Fig. 2(a) is the band structure of a pristine  $\text{TiS}_3$  monolayer. While the PBE underestimates the band gap by giving a value of 0.30 eV at the  $\Gamma$  point, the HSE increases it to 1.15 eV but holds its direct-gap feature. We also calculate the parity for band-edge states as denoted. Being the same odd parity implies that transitions between them are dipole forbidden, which suppresses system screening and decouples the exciton binding energy from the band gap. This has been shown to play a key role in the spontaneous formation of

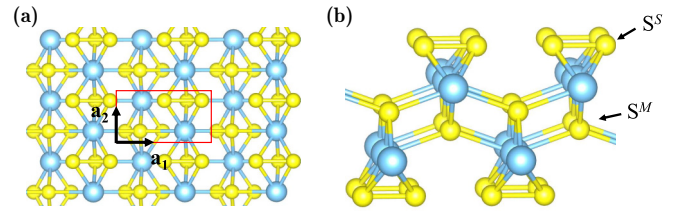


FIG. 1. (a) Top and (b) side views of monolayer  $\text{TiS}_3$ . Cyan and yellow balls denote Ti and S atoms, respectively. The red rectangle denotes the unit cell with in-plane lattice vectors  $\mathbf{a}_1$  and  $\mathbf{a}_2$ .

exciton condensation [12]. Here, the obtained results are in line with previous studies [12,17,45].

In order to maintain a well-defined parity, only Se substitutions that can preserve inversion symmetry are considered throughout the paper. According to the location of Se, there are three cases, namely, (i) two Se replace two side S [denoted as  $\text{TiS}_2\text{Se}^S$ ; see the inset of Fig. 2(b)], (ii) four Se replace all four side S [denoted as  $\text{TiSSe}_2$ ; see the inset of Fig. 2(c)], and (iii) two Se replace two middle S [denoted as  $\text{TiS}_2\text{Se}^M$ ; see the inset of Fig. 2(d)].

Their corresponding electronic structures are plotted in Figs. 2(b)–2(d). First, we find that the parity of band-edge states remains unchanged regardless of where the Se appears. At the PBE level, both  $\text{TiS}_2\text{Se}^S$  and  $\text{TiSSe}_2$  are characterized by an indirect gap with values of 0.33 and 0.13 eV, respectively. But  $\text{TiS}_2\text{Se}^M$  is predicted to be metallic with a small overlap between the bottom conduction band and top valence band. Actually, the PBE significantly underestimates the band gap of bulk and monolayer  $\text{TiS}_3$  [17], which should be also the case for the alloys. Previous work showed that the HSE can reproduce the experiment gap for  $\text{TiS}_3$  [16,17]. Herein, the HSE increases the minimum gap to 1.18, 0.76, and 0.58 eV for  $\text{TiS}_2\text{Se}^S$ ,  $\text{TiSSe}_2$ , and  $\text{TiS}_2\text{Se}^M$ . The former two are still indirect, which are, respectively, 0.03 and 0.25 eV smaller than the direct gap at the  $\Gamma$  point, while the latter is direct at the  $\Gamma$  point.

These results indicate that the change in the band gap strongly depends on the Se substitution position. A comparison between Figs. 2(a) and 2(b) reveals that when only part of the  $S^S$  is replaced, the gap is hardly affected and the change in the band structure mostly occurs at the  $X$  point. But further increasing the Se concentration would lead to a notable minimum-gap reduction due to the gradual downshift of the conduction band at the  $X$  point.  $\text{TiSSe}_2$  is a case in which all the  $S^S$  is replaced by Se, and the HSE gap is decreased by 0.39 eV relative to that of  $\text{TiS}_3$ . For comparison, the change in the direct gap is not so obvious. In contrast, replacing  $S^M$  significantly reduces the HSE band gap to only about half that of  $\text{TiS}_3$  (see Table I). The two categories of gap reduction above should be associated with different physical origins [33].

Both our calculations and previous works [18,45] show that the top valence band of monolayer  $\text{TiS}_3$  is dominantly contributed from  $S^M$ . So when these  $S^M$  atoms are replaced by the less electronegative Se atoms, the valence band moves upwards, certainly giving rise to a smaller band gap for  $\text{TiS}_2\text{Se}^M$ . Likewise, replacing a fraction of  $S^S$  atoms barely affects the

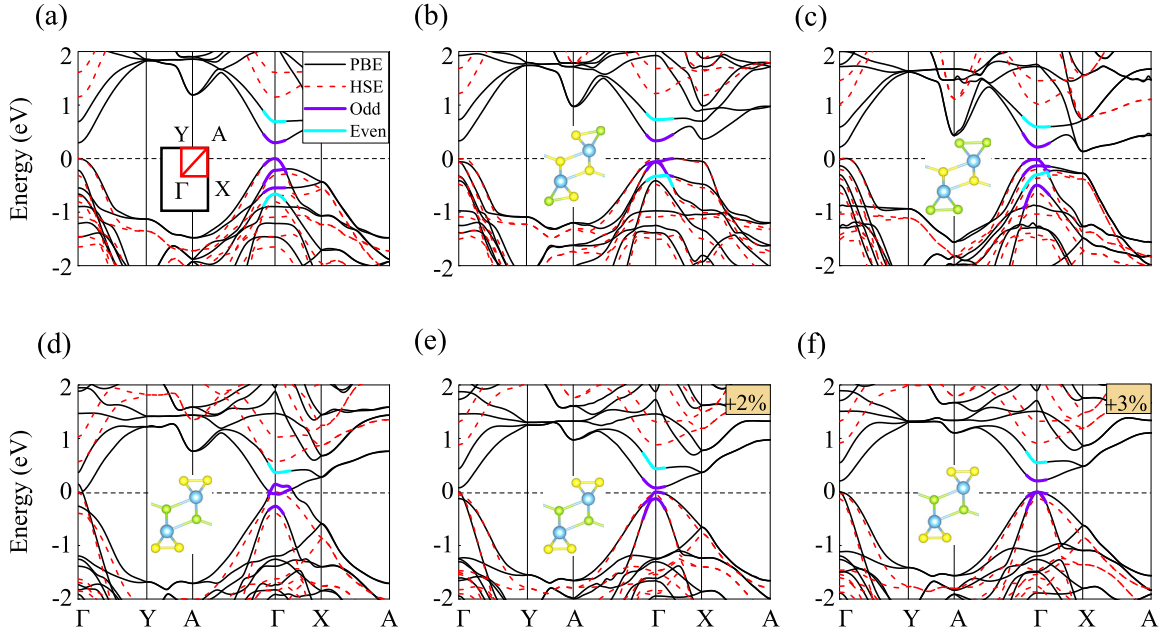


FIG. 2. Electronic structures of (a)  $\text{TiS}_3$ , (b)  $\text{TiS}_2\text{Se}^S$ , (c)  $\text{TiSSe}_2$ , (d)  $\text{TiS}_2\text{Se}^M$ , (e)  $\text{TiS}_2\text{Se}^M$  with 2% strain, and (f)  $\text{TiS}_2\text{Se}^M$  with 3% strain. Black solid lines are calculated by PBE and red dashed lines are by HSE06. Band parities are also denoted for the states close to the Fermi level which is set to energy zero. Shown in the inset of (a) is the Brillouin zone for band structure calculations. Shown in the insets of (b)–(f) are the corresponding geometric configurations. Cyan, yellow, and orange balls are Ti, S, and Se atoms.

band-edge state, so the band gap is basically unchanged. This is the case for  $\text{TiS}_2\text{Se}^S$ . But on the other hand, Se has a larger atomic radius than that of S. If too many Se atoms appear at the side, there is not enough space to allow their sufficient relaxation, hence introducing an internal pressure. This is another alternative mechanism that can lead to a gap reduction [12]. Some hints might be unveiled from the change in lattice constant as compared in Table I.  $\text{TiS}_2\text{Se}^S$  has almost the same  $a_1$  as  $\text{TiS}_3$  and  $a_2$  is slightly increased by  $\sim 1.5\%$ . But from  $\text{TiS}_2\text{Se}^S$  to  $\text{TiSSe}_2$ ,  $a_1$  is remarkably increased by  $\sim 4.3\%$ , meaning there is insufficient room for the larger Se-Se dimer (see Fig. 1). Then a compressive strain is introduced and the gap reduction should be largely related to a “geometrical” effect, unlike the “electronic” effect for  $\text{TiS}_2\text{Se}^M$ .

Before exploring the excitonic properties, it is worth noting that  $\text{TiS}_2\text{Se}^M$  shows a metallic behavior by the PBE. Although the HSE can produce a band gap, at present, it is computationally unsustainable to solve the BSE on the HSE level. Directly applying a scissor correction on a metallic band is

problematic. Herein we apply a small in-plane strain to fix this issue. As shown in Figs. 2(e) and 2(f), a gap of 0.08 and 0.21 eV is opened under 2% and 3% strain at the  $\Gamma$  point, respectively. Except for the gap opening, just a slight change is found in comparison with the band structure plotted in Fig. 2(d) which is the one without strain. Below, we will first discuss the excitonic properties of  $\text{TiS}_2\text{Se}^M$  by solving the BSE on the 2%-strained electronic structure from the PBE but with a scissor correction to the HSE band gap of pristine  $\text{TiS}_2\text{Se}^M$ , namely, 0.58 eV.

In Fig. 3 and Table I, we compare the low-energy excitations of  $\text{TiS}_3$  and the alloys. Because band-edge transitions are dipole forbidden, the ground-state exciton  $X_1$  is dark for all four situations. Forming this exciton costs an energy of 0.4 eV for pristine  $\text{TiS}_3$ , in agreement with the published literature [12]. This value changes slightly to 0.48 eV for  $\text{TiS}_2\text{Se}^S$  and is reduced to half, 0.2 eV, for  $\text{TiSSe}_2$ . In sharp contrast, it becomes negative, namely,  $-0.13$  eV for  $\text{TiS}_2\text{Se}^M$  as shown in Fig. 3(d), which means spontaneous

TABLE I. Comparison of lattice constant, minimum gap, direct gap at the  $\Gamma$  point, formation energy ( $E_f$ ), and corresponding binding energy ( $E_b$ ) of the ground-state  $X_1$  exciton, as well as two-dimensional polarizability ( $\alpha_{2D}$ ), for the  $\text{TiS}_{3-x}\text{Se}_x$ . Note that the  $E_f$  and  $E_b$  for the  $\text{TiS}_2\text{Se}^M$  are obtained on the electronic structure under 2% strain but correcting the band gap by a scissor operator to the HSE06 value without strain, namely, 0.58 eV.

	Lattice constant ( $\text{\AA}$ )		Minimum gap (eV)		Direct gap (eV)		$E_f$ (eV)	$E_b$ (eV)	$\alpha_{2D}$ ( $\text{\AA}$ )
	$a_1$	$a_2$	PBE	HSE06	PBE	HSE06			
$\text{TiS}_3$	5.017	3.413	0.30	1.15	0.30	1.15	0.40	0.75	5.66
$\text{TiS}_2\text{Se}^S$	5.018	3.465	0.33	1.18	0.39	1.21	0.48	0.73	6.44
$\text{TiSSe}_2$	5.232	3.495	0.13	0.76	0.21	1.01	0.20	0.81	6.74
$\text{TiS}_2\text{Se}^M$	5.188	3.455	Metal	0.58	Metal	0.58	$-0.13$	0.71	6.13



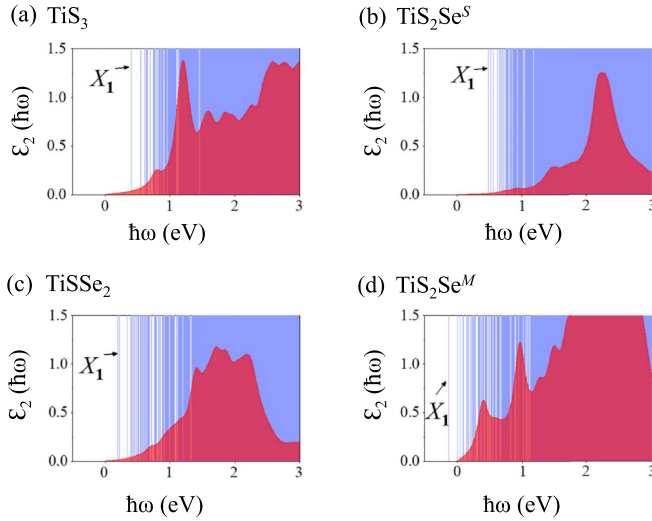


FIG. 3. Exciton energies (blue vertical lines) superimposed on the imaginary part ( $\epsilon_2$ ) of the BSE dielectric function in the low-energy region for the (a)  $\text{TiS}_3$ , (b)  $\text{TiS}_2\text{Se}^S$ , (c)  $\text{TiSSe}_2$ , and (d)  $\text{TiS}_2\text{Se}^M$ .  $X_1$  denotes the ground-state exciton with the lowest formation energy. A negative energy means spontaneous formation of the corresponding exciton.

generation of the  $X_1$  exciton. In other words, the one-electron band structure becomes unstable against the transition to an excitonic insulator [5]. Although both  $\text{TiS}_2\text{Se}^S$  and  $\text{TiSSe}_2$  exhibit an indirect-gap feature, there is only a rather small difference between their direct and indirect gaps. In this regard, that we consider a zero-momentum exciton should hardly impact the real formation energy of the ground-state exciton.

It is instructive to analyze in detail the trend that distinct Se substitutions lead to different excitonic properties. By definition, the exciton formation energy is the net difference between the exciton binding energy and the corresponding one-electron gap. Accordingly, the exciton binding energies are derived and summarized in Table I. Interestingly, they are all in the range 0.71–0.81 eV. As compared with the notable change in the band gap, the exciton binding energy can be considered to be almost constant, independent of the concentration and position of Se substitution. Therefore, it is the disproportional effect of Se alloying on the one-electron band gap and many-body interaction of the system that triggers the excitonic instability in  $\text{TiS}_2\text{Se}^M$ .

To better understand the Se alloying effect on the system's electron-hole interaction, we plot the real-space exciton wave functions for the four cases in Fig. 4. In appearance, the wave functions of  $\text{TiS}_3$  and  $\text{TiSSe}_2$  are similar: The electron is distributed in a circular fashion around the hole. The wave functions of  $\text{TiS}_2\text{Se}^S$  and  $\text{TiS}_2\text{Se}^M$  are similar: The electron is distributed in a quasi-one-dimensional fashion relative to the hole, along the  $a_2$  direction. Previous works [21,46] showed the importance of two-dimensional polarizability in determination of the electron-hole screening interaction, as well as the binding energy of two-dimensional excitons. Our calculations yield values of 5.66, 6.44, 6.74, and 6.13 Å for monolayer  $\text{TiS}_3$ ,  $\text{TiS}_2\text{Se}^S$ ,  $\text{TiSSe}_2$ , and  $\text{TiS}_2\text{Se}^M$ . Indeed, the

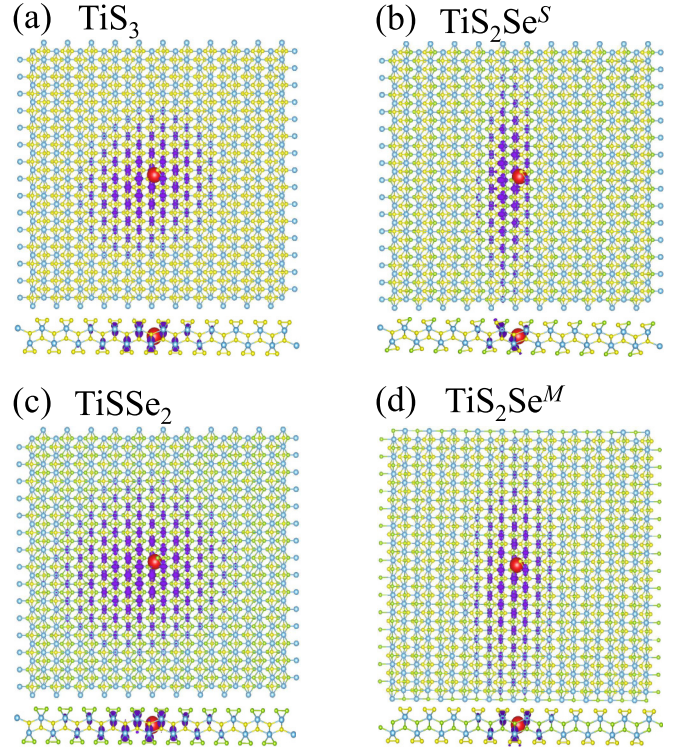


FIG. 4. Real-space wave-function plots of the  $X_1$  exciton for the (a)  $\text{TiS}_3$ , (b)  $\text{TiS}_2\text{Se}^S$ , (c)  $\text{TiSSe}_2$ , and (d)  $\text{TiS}_2\text{Se}^M$ . The hole is fixed at the center (red ball) and the isosurface corresponds to the electron density of  $0.06 e/\text{\AA}^3$ .

change in two-dimensional polarizability is not large, implying a relatively small change in the system screening effect. However, the trend of its relative size does not correspond to the relative size of the exciton binding energy (see Table I). This is probably due to the dark-exciton nature while the reported quantitative relationship between the exciton binding energy and two-dimensional polarizability is applicable to the optically active bright excitons [21,46].

Next, we discuss the approximation to calculate the excitonic properties of  $\text{TiS}_2\text{Se}^M$  in terms of the electronic structure under 2% strain. First, a comparison between the HSE bands without and with strain [see Figs. 2(d) and 2(e)] reveals little difference. Furthermore, we calculated the electronic structure under 3% strain which is shown in Fig. 2(f). It has a direct gap of 0.21/0.94 eV at the PBE/HSE level. On the basis of this PBE band, solving the BSE with a scissor correction to the HSE gap (0.94 eV) leads to an exciton formation energy of 0.20 eV. The value is almost identical to 0.21 eV which is obtained from the PBE band under 2% strain coupled with a scissor correction to the gap of 0.94 eV. The almost identical value is indicative of a negligible effect of small strain on the formation energy of the  $X_1$  exciton. The corresponding exciton binding energies are also further deduced, namely, 0.74 and 0.73 eV, respectively, for the two calculating means. Again, they both fall within the aforementioned 0.71–0.81 eV range. Note that a similar weak strain dependence of the exciton binding energy is also found in monolayer  $\text{TiS}_3$  [12]. Altogether, the negative exciton formation energy of  $-0.13$  eV

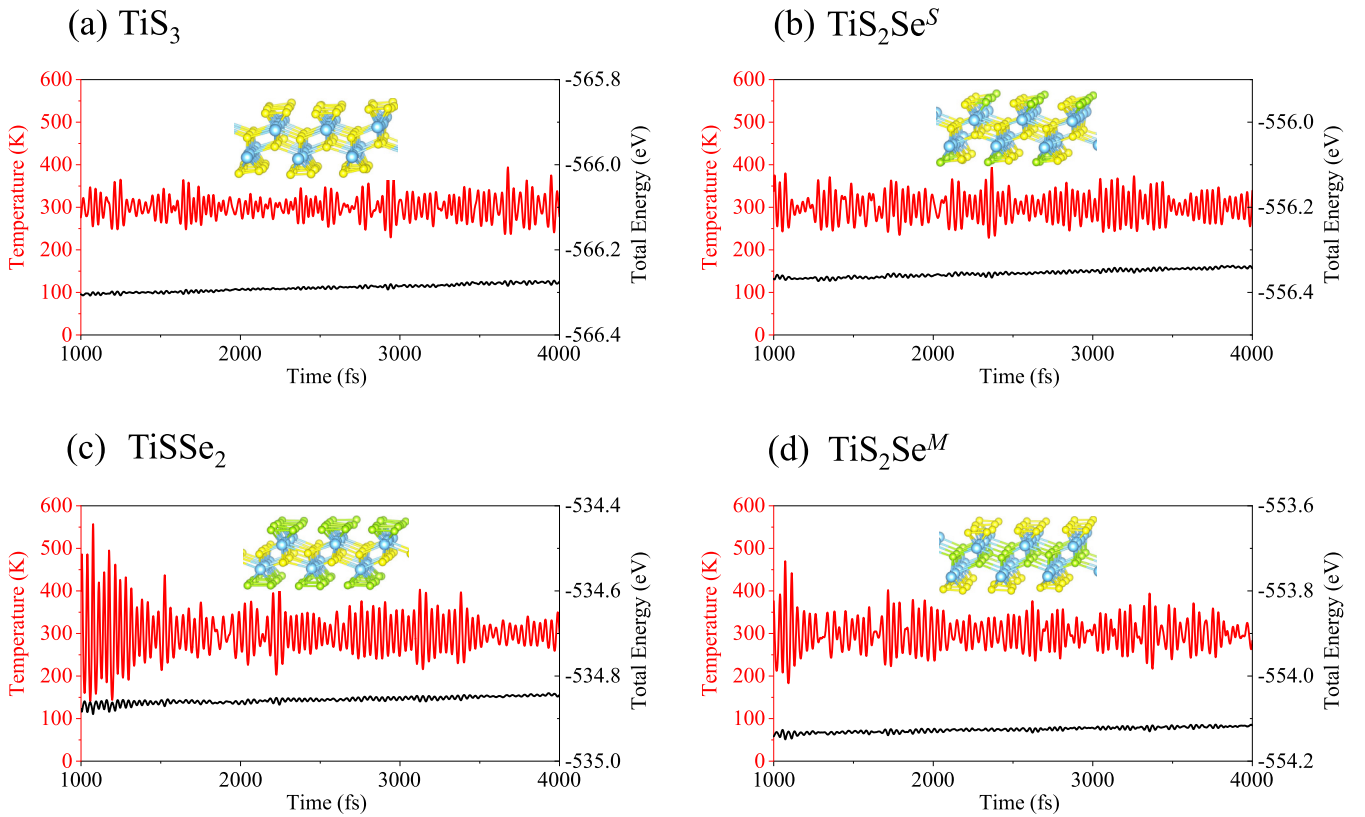


FIG. 5. Temperature and energy fluctuations with the time step for (a)  $\text{TiS}_3$ , (b)  $\text{TiS}_2\text{Se}^S$ , (c)  $\text{TiSSe}_2$ , and (d)  $\text{TiS}_2\text{Se}^M$ . Insets are the corresponding structures at 4 ps.

should be quite reasonable for  $\text{TiS}_2\text{Se}^M$ , and therefore the excitonic instability.

Experimentally, Se has been successfully alloyed into  $\text{TiS}_3$ , although in appearance, our studied cases correspond to a relatively large amount of Se alloying as compared with the current experimental observation [37]. Two reasons lead us to believe that our model can capture the underlying physics for the occurrence of the excitonic instability in a  $\text{TiS}_{3-x}\text{Se}_x$  alloy. On the one hand, the energetics showed that the most stable alloy composition is located at  $x = 1/3$  for  $\text{TiS}_{3-x}\text{Se}_x$  [37], which just corresponds to the compounds  $\text{TiS}_2\text{Se}^S$  and  $\text{TiS}_2\text{Se}^M$  studied here. In practice, the higher amount of alloying of Se might be alternatively obtained by means of other nonequilibrium methods, as will be discussed later in the basis of defect engineering. On the other hand, the effect of Se concentration seems marginal in comparison with that from its substitution position. For instance, we performed calculations on the case of only one Se substitution for one side S. Now the Se concentration is half that of  $\text{TiS}_2\text{Se}^S$ . But the results (not shown here) are essentially similar to those of  $\text{TiS}_2\text{Se}^S$ , both in terms of the one-electron band structure and excitonic properties.

In this sense, the location of Se becomes critical to the phase transition from a band insulator to an excitonic insulator, i.e., Se needs to replace the middle S. Here, we give some hints by comparing the energetics of different  $\text{TiS}_{3-x}\text{Se}_x$  ( $x = 0, 1$ , and 2) alloys. The  $\text{TiS}_2\text{Se}^M$  has a higher energy by 74 meV/Se than that of  $\text{TiS}_2\text{Se}^S$ , so Se prefers to replace the side S under a small alloying concentration. This makes sense

because there is more space on the edges to accommodate larger Se atoms, consequently lowering the system's total energy. Nevertheless, going from  $\text{TiS}_2\text{Se}^S$  to  $\text{TiSSe}_2$  costs an additional energy of 580 meV/Se as compared to going from  $\text{TiS}_3$  to  $\text{TiS}_2\text{Se}^S$ . Such an energy requirement is too much as compared to 74 meV/Se which is the corresponding amount to replace the middle S. Hence, there must be a thermodynamically stable  $\text{TiS}_{3-x}\text{Se}_x$  alloy phase in which  $S^M$  has been replaced by Se before it becomes  $\text{TiSe}_3$ . In addition, given that the Se-to- $S^M$  substitution only costs an additionally moderate energy of 74 meV/Se than the Se-to- $S^S$  substitution, there might be some kind of dynamical control in experiment to solely replace the  $S^M$  and directly fabricate the desired  $\text{TiS}_2\text{Se}^M$  structure. One possible route is to first create a single S vacancy in  $\text{TiS}_3$  using methods that have proven to be successful in other transition-metal sulfides, such as oxygen plasma exposure [47] and electrochemical desulfurization [48], and then saturate these S vacancies with Se atoms. Our calculations show that Se prefers to bind the S vacancy at the middle rather than at the side as a result of a larger binding energy by  $\sim 2$  eV. In this way, Se can be incorporated into the desired middle site.

We further test the system's stability by molecular dynamic calculations for the four studied systems as implemented in the Vienna *ab initio* simulation package (VASP) [49]. The time step is set to be 1 fs and the simulation lasts 4 ps at 300 K using the Nosé algorithm. Figure 5 shows the temperature and energy fluctuations for the last 3 ps, which is consistent with the observation that the quintuple-layer structure

of  $\text{TiS}_{3-x}\text{Se}_x$  is always preserved in the molecular dynamic simulations. Hence, we can expect that  $\text{TiS}_{3-x}\text{Se}_x$  should be stable with respect to thermal fluctuations up to room temperature.

#### IV. CONCLUSIONS

In summary, first-principles calculations in combination with the Bethe-Salpeter equation reveal the possibility of engineering an excitonic insulator via alloying Se into a  $\text{TiS}_3$  monolayer. The physics behind this lies in the distinct responses of electrons and excitons to the Se substitution. While the electronic band gap can be significantly decreased, the

exciton binding energy varies slightly. Replacing Se for the middle S atoms will lead to spontaneous exciton formation as now the one-electron band gap has been reduced to less than the exciton binding energy. The energetic calculations demonstrate the feasibility of alloying Se at the desired middle site. Our work offers insight for engineering an excitonic insulator in two-dimensional materials.

#### ACKNOWLEDGMENTS

We acknowledge useful discussions with Zeyu Jiang. This work was supported by the National Natural Science Foundation of China (Grant No. 11674071) and the Beijing Institute of Technology Research Fund Program for Young Scholars.

- 
- [1] N. F. Mott, *Philos. Mag.* **6**, 287 (1961).
  - [2] R. X. Knox, in *Solid State Physics*, edited by F. Seitz and D. Turnbull (Academic, New York, 1963), Suppl. 5, p. 100.
  - [3] L. V. Keldysh and Yu. V. Kopaev, *Fiz. Tverd. Tela* **6**, 2791 (1964) [*Sov. Phys.-Solid State* **6**, 2219 (1965)].
  - [4] J. DesCloizeaux, *J. Phys. Chem. Solids* **26**, 259 (1965).
  - [5] D. Jérôme, T. M. Rice, and W. Kohn, *Phys. Rev.* **158**, 462 (1967).
  - [6] B. I. Halperin and T. M. Rice, *Rev. Mod. Phys.* **40**, 755 (1968).
  - [7] A. Kogar, S. Vig, M. S. Rak, A. A. Husain, F. Flicker, Y. I. Joe, L. Venema, G. J. MacDougall, T. C. Chiang, E. Fradkin, J. van Wezel, and P. Abbamonte, *Science* **358**, 1314 (2017).
  - [8] L. J. Du, X. W. Li, W. K. Lou, G. Sullivan, K. Chang, J. Kono, and R. R. Du, *Nat. Commun.* **8**, 1971 (2017).
  - [9] Z. F. Wang, D. A. Rhodes, K. Watanabe, T. Taniguchi, J. C. Hone, J. Shan, and K. F. Mak, *Nature (London)* **574**, 76 (2019).
  - [10] Z. Li, M. Nadeem, Z. J. Yue, D. Cortie, M. Fuhrer, and X. L. Wang, *Nano Lett.* **19**, 4960 (2019).
  - [11] D. Varsano, S. Sorella, D. Sangalli, M. Barborini, S. Corni, E. Molinari, and M. Rontani, *Nat. Commun.* **8**, 1461 (2017).
  - [12] Z. Y. Jiang, Y. C. Li, S. B. Zhang, and W. H. Duan, *Phys. Rev. B* **98**, 081408(R) (2018).
  - [13] D. Varsano, M. Palummo, E. Molinari, and M. Rontani, *Nat. Nanotechnol.* **15**, 367 (2020).
  - [14] Z. Y. Jiang, Y. C. Li, W. H. Duan, and S. B. Zhang, *Phys. Rev. Lett.* **122**, 236402 (2019).
  - [15] Z. Y. Jiang, W. K. Lou, Y. Liu, Y. C. Li, H. F. Song, K. Chang, W. H. Duan, and S. B. Zhang, *Phys. Rev. Lett.* **124**, 166401 (2020).
  - [16] J. O. Island, M. Barawi, R. Biele, A. Almazán, J. M. Clamagirand, J. R. Ares, C. Sánchez, H. S. J. van der Zant, J. V. Álvarez, R. D'Agosta, I. J. Ferrer, and A. Castellanos-Gomez, *Adv. Mater.* **27**, 2595 (2015).
  - [17] J. Dai and X. C. Zeng, *Angew. Chem., Int. Ed.* **54**, 7572 (2015).
  - [18] J. Zhang, X. L. Liu, Y. W. Wen, L. Shi, R. Chen, H. J. Liu, and B. Shan, *ACS Appl. Mater. Interfaces* **9**, 2509 (2017).
  - [19] A. Khatibi, R. H. Godiksen, S. B. Basuvalingam, D. Pellegrino, A. A. Bol, B. Shokri, and A. G. Curto, *2D Mater.* **7**, 015022 (2020).
  - [20] A. J. Molina-Mendoza, M. Barawi, R. Biele, E. Flores, J. R. Ares, C. Sánchez, G. Rubio-Bollinger, N. Agrait, R. D'Agosta, I. J. Ferrer, and A. Castellanos-Gomez, *Adv. Electron. Mater.* **1**, 1500126 (2015).
  - [21] Z. Y. Jiang, Z. R. Liu, Y. C. Li, and W. H. Duan, *Phys. Rev. Lett.* **118**, 266401 (2017).
  - [22] M. Van der Donck and F. M. Peeters, *Phys. Rev. B* **98**, 235401 (2018).
  - [23] E. Torun, H. Sahin, A. Chaves, L. Wirtz, and F. M. Peeters, *Phys. Rev. B* **98**, 075419 (2018).
  - [24] F. Ersan and C. Ataca, *Phys. Rev. Appl.* **13**, 064008 (2020).
  - [25] R. Mahat, K. C. Shambhu, D. Wines, F. Ersan, S. Regmi, U. Karki, R. White, C. Ataca, P. Padhan, A. Gupta, and P. LeClair, *J. Alloys Compd.* **830**, 154403 (2020).
  - [26] I. Miyazato, S. Sarikurt, K. Takahashi, and F. Ersan, *J. Mater. Sci.* **55**, 660 (2020).
  - [27] F. Ersan, G. Gökoğlu, and E. Aktürk, *J. Phys. Chem. C* **119**, 28648 (2015).
  - [28] G. Wang, C. Robert, A. Suslu, B. Chen, S. J. Yang, S. Alamdari, I. C. Gerber, T. Amand, X. Marie, S. Tongay, and B. Urbaszek, *Nat. Commun.* **6**, 10110 (2015).
  - [29] H. Bragança, F. Riche, F. Qu, V. Lopez-Richard, and G. E. Marques, *Sci. Rep.* **9**, 4575 (2019).
  - [30] Y. F. Chen, D. O. Dumcenco, Y. M. Zhu, X. Zhang, N. N. Mao, Q. L. Feng, M. Zhang, J. Zhang, P.-H. Tan, Y.-S. Huang, and L. M. Xie, *Nanoscale* **6**, 2833 (2014).
  - [31] Y. P. Liu, K. Tom, X. W. Zhang, S. Lou, Y. Liu, and J. Yao, *New J. Phys.* **19**, 073018 (2017).
  - [32] M. Yagmurcukardes and F. M. Peeters, *Phys. Rev. B* **101**, 155205 (2020).
  - [33] F. Ersan, H. D. Ozaydin, and E. Aktürk, *Phys. Chem. Chem. Phys.* **20**, 1431 (2018).
  - [34] L. M. Xie, *Nanoscale* **7**, 18392 (2015).
  - [35] Y. Oshima, Y. Nakamura, K. Tezuka, and Y. J. Shan, *ChemistrySelect* **5**, 2588 (2020).
  - [36] T. L. Tan, M.-F. Ng, and G. Eda, *J. Phys. Chem. C* **120**, 2501 (2016).
  - [37] A. Agarwal, Y. Qin, B. Chen, M. Blei, K. D. Wu, L. Liu, Y. X. Shen, D. Wright, M. D. Green, H. L. Zhuang, and S. Tongay, *Nanoscale* **10**, 15654 (2018).
  - [38] J. P. Perdew, K. Burke, and M. Ernzerhof, *Phys. Rev. Lett.* **77**, 3865 (1996).

- [39] P. Giannozzi, S. Baroni, N. Bonini, M. Calandra, R. Car, C. Cavazzoni, D. Ceresoli, G. L. Chiarotti, M. Cococcioni, I. Dabo, A. D. Corso, S. de Gironcoli, S. Fabris, G. Fratesi, R. Gebauer, U. Gerstmann, C. Gougoussis, A. Kokalj, M. Lazzeri, L. Martin-Samos *et al.*, *J. Phys.: Condens. Matter* **21**, 395502 (2009).
- [40] J. Heyd, G. E. Scuseria, and M. Ernzerhof, *J. Chem. Phys.* **118**, 8207 (2003); J. Heyd and G. E. Scuseria, *ibid.* **124**, 219906 (2006).
- [41] D. R. Hamann, *Phys. Rev. B* **88**, 085117 (2013).
- [42] A. Marini, C. Hogan, M. Grüning, and D. Varsano, *Comput. Phys. Commun.* **180**, 1392 (2009).
- [43] D. Sangalli, A. Ferretti, H. Miranda, C. Attaccalite, I. Marri, E. Cannuccia, P. Melo, M. Marsili, F. Paleari, A. Marrazzo, G. Prandini, P. Bonfa, M. O. Atambo, F. Affinito, M. Palumbo, A. Molina-Sanchez, C. Hogan, M. Grüning, D. Varsano, and A. Marini, *J. Phys.: Condens. Matter* **31**, 325902 (2019).
- [44] K. Momma and F. Izumi, *J. Appl. Crystallogr.* **44**, 1272 (2011).
- [45] J. Kang and L. W. Wang, *Phys. Chem. Chem. Phys.* **18**, 14805 (2016).
- [46] T. Olsen, S. Latini, F. Rasmussen, and K. S. Thygesen, *Phys. Rev. Lett.* **116**, 056401 (2016).
- [47] G. Ye, Y. Gong, J. Lin, B. Li, Y. He, S. T. Pantelides, W. Zhou, R. Vajtai, and P. M. Ajayan, *Nano Lett.* **16**, 1097 (2016).
- [48] C. Tsai, H. Li, S. Park, J. Park, H. S. Han, J. K. Nørskov, X. Zheng, and F. Abild-Pedersen, *Nat. Commun.* **8**, 15113 (2017).
- [49] G. Kresse and J. Furthmüller, *Phys. Rev. B* **54**, 11169 (1996).